Communication-Free Pulsed Power Distribution and Tracking Method for Hybrid Energy Storage System Based on Active Disturbance Rejection Control

Lunbo Deng, *Student Member, IEEE*, Guohua Zhou, *Senior Member, IEEE*, Yanglong Li,
and Zhengge Chen, *Member, IEEE*

***Abstract*—A dc microgrid is encountering the stability issues caused by emerging pulsed power loads (PPLs). A hybrid energy storage system (HESS) helps to suppress dc bus fluctuation due to periodical power demand of PPL within a short time. A common practice is to handle transient and steady power separately with high-power-density and high-energy-density units. This article proposes a novel communication-free pulsed power distribution method for the HESS consisting of battery and supercapacitor (SC) units; the battery unit only provides dc power, while the SC unit provides an ac component of pulsed power. To track the high-frequency ac component, active disturbance rejection control (ADRC) is applied to the SC unit. Taking dual-active-bridge converters as the interfaces, a detailed design process is presented. Besides, the frequency-domain model illustrates the mechanism of dc–ac power distribution, and a comparison with proportional–integral control shows the advantage of ADRC in fast ac power tracking. With the proposed control strategy, the current surge to the battery unit is significantly reduced and the droop characteristics are unaffected when PPL works. Finally, an HESS testbench supplying 10–150 Hz 1 kW PPL is built to verify the proposed pulsed power distribution and tracking method.**

***Index Terms*—Active disturbance rejection control (ADRC), dual-active-bridge (DAB) converter, hybrid energy storage system (HESS), power distribution, pulsed power load (PPL).**

I. INTRODUCTION

ENERGY and environmental concerns give rise to the development of a microgrid that integrates a distributed generator (DG), an energy storage system (ESS), and loads. The technology of dc microgrid is receiving increasing attention because there are no issues on reactive power and frequency regulation; hence, keeping the stability of dc bus voltage through the ESS and its interface converter is the priority [1], [2].

However, with a variety of loads connecting to the dc microgrid, controlling the bus within an acceptable voltage is becoming a challenge. The power pulsed loads (PPLs), such as industrial electrolysis, electroplating, wastewater purifying, phased-array radar, and plasma source device [3], [4], [5], have the features of instantaneous and periodical peak power and may deviate the dc bus from its rated voltage. Although they are usually equipped with dedicated pulsed power supplies, the pulsed current inevitably flows into the dc bus, leading to voltage fluctuation. It is feasible but not economic to parallel high-capacity capacitors to the bus, while it also brings the risk of high short-circuit current. Another approach is to employ the ESS to balance the power difference, which requires an appropriate controller with fast-tracking ability. The linear–quadratic regulator (LQR) control with state feedback demonstrates the performance beyond proportional–integral (PI) control; however, its dynamic performance is degraded when high parameter uncertainties exist [6]. Model-predictive control (MPC) exhibits very fast response performance and is applied to the battery ESS for supporting shipboard dc microgrid [7], making the bus voltage almost immune to 20 Hz PPL. However, there is still a paradox that the less the bus voltage is affected, the more pulsed power the ESS provides, which greatly reduces the battery life [8]. Hence, an auxiliary energy storage device is needed to improve the robustness of bus voltage and, meanwhile, reduce the impact on battery service life from PPL. A supercapacitor (SC) unit is usually preferred because of its high-power-density and durable properties [9].

Effective power distribution is essential to a hybrid energy storage system (HESS). Most research works treat the HESS as a whole; namely, the two interface converters share all information. The method based on a low-pass filter (LPF) is widely used; the battery controller calculates the total power demand and then sends the transient power reference to the SC controller [10]. An HESS optimization strategy is applied to minimize energy consumption [11], but stabilizing the bus voltage is not the primary goal. MPC-based and deadbeat-control (DBC)-based hybrid power sources are proposed in [12] and [13], respectively. They both need a high-speed central processing unit to calculate the optimal power distribution and maintain bus voltage; however, the heavy calculation burden limits their applications in high-frequency converters. A virtual impedance [14] and a virtual notch filter [15] are proposed to suppress the bus voltage fluctuation; they both take a load current feedforward

---

Manuscript received 28 July 2023; revised 13 October 2023; accepted 17 November 2023. Date of publication 24 November 2023; date of current version 26 January 2024. This work was supported by the National Natural Science Foundation of China under Grant 62271417. Recommended for publication by Associate Editor S. Khajehoddin. *(Corresponding author: Guohua Zhou.)*

The authors are with the School of Electrical Engineering, Southwest Jiaotong University, Chengdu 611756, China (e-mail: denglb_pece@my.swjtu.edu.cn; eeghzhou@swjtu.edu.cn; lylswjtu@my.swjtu.edu.cn; zgc@swjtu.edu.cn).

Color versions of one or more figures in this article are available at https://doi.org/10.1109/TPEL.2023.3336511.

Digital Object Identifier 10.1109/TPEL.2023.3336511

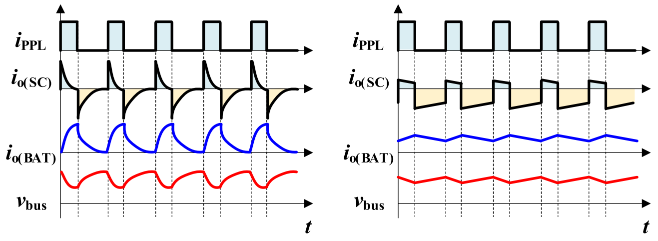

(a) (b)

Fig. 1. Power distribution methods for the HESS. (a) Steady–transient distribution. (b) DC–AC distribution.

technique and introduce pulsed current into specific capacitor packs. The abovementioned strategies share information of all power conversion units, which requires that the two kinds of energy storage units must be installed very near to each other for real-time communication and information exchange.

Owing to the distributed property of a dc microgrid, the distributed and decentralized control strategies through local calculation instead of centralized calculation are developed. A hierarchical control of HESS is proposed for both the centralized and distributed cases, proving that centralized control has higher control accuracy but suffers from lower reliability in case of communication delay and failure [16]. The concept of virtual capacitor is introduced into droop control, which takes the integral value of the output current into the closed-loop feedback path; when the load current changes, the SC converter could respond transient power immediately, and the battery converter responds the steady part [17], [18], [19].

However, the existing methods for the HESS supplying PPL do not utilize the full capacity of the SC. As shown in Fig. 1(a), when supplying PPL, the output current of the battery converter $i_{\mathrm{o(BAT)}}$ supplies a large periodical component, and the output current of the SC converter $i_{\mathrm{o(SC)}}$ only exists for a short time. It means that the battery still provides the peak power; besides, a battery unit with such a large capacity is much more expensive than the SC unit [20]. What is more, the droop characteristics of the battery converter would cause periodical fluctuation to the dc bus. This kind of power distribution method is called steady–transient distribution in this article.

The concept of dc–ac power distribution that was used in pulsed power supplies [21] is a potential solution for the issues by steady–transient distribution. The dc–ac power distribution is illustrated in Fig. 1(b). The SC converter provides most of the ac current, leading to higher utilization of SC and less bus fluctuation; meanwhile, the current surge to the battery unit is greatly reduced.

The challenges are that the HESS is communication-free in a distributed dc microgrid, and the total load current is not easy to obtain. In addition, dc–ac distribution needs a high-bandwidth control strategy for high-frequency ac current tracking.

The main contributions of this article are as follows.

1) Through the proposed current estimator, communication-free control is realized with only local measurement.
2) The concept of dc–ac distribution is first introduced in the dc microgrid with the HESS, with a detailed design process.
3) The reduction of dc bus fluctuation by PPL is explained by a frequency-domain model, which consists of impedance and a newly defined controlled current source.

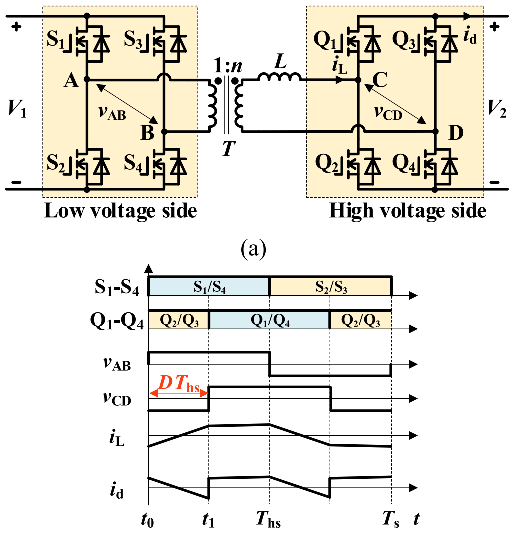

(a)

(b)

Fig. 2. DAB converter. (a) Circuit. (b) Key waveforms.

The rest of this article is organized as follows. In Section II, an HESS with a dual-active-bridge (DAB) converter as the interface is established, and the load current estimation and ac current extraction algorithm are presented. In Section III, the SC controller design based on active disturbance rejection control (ADRC) [22] is derived, and the SC converter could perform as a current source automatically tracking the ac component. In Section IV, the frequency-domain analysis explains the power distribution mechanism in this application. Section V verifies the proposed pulsed power distribution and tracking method with a low-voltage testbench. In Section VI, detailed comparisons related to power distribution and tracking methods are provided. Finally, Section VII concludes this article.

II. SYSTEM SIMPLIFICATION AND AC POWER ESTIMATION

A. Architecture of HESS With DAB Interface Converters

The circuit of the DAB converter is depicted in Fig. 2(a); there are two full bridges and an auxiliary inductor L set in high-voltage side. Fig. 2(b) presents the waveforms with single-phase-shift modulation, the switches in each half-bridge are complementary, and $\mathrm{S}_1/\mathrm{S}_3$ and $\mathrm{Q}_1/\mathrm{Q}_3$ are complementary. Define D as the phase-shift ratio, T_{hs} as half a switching period, and the time difference DT_{hs} between S_1 and Q_1 changes inductor current i_{L}, rectified current i_{d}, and power flow. The transferred power from V_1 to V_2 is as follows [23]:

$$P = \begin{cases} \frac{nV_1V_2}{2f_{\mathrm{s}}L}D(1-D), & D\in[0,\ 0.5] \\ \frac{nV_1V_2}{2f_{\mathrm{s}}L}D(1+D), & D\in[-0.5,\ 0] \end{cases} \tag{1}$$

where n is the turn ratio of the transformer and f_{s} is the switching frequency. Positive and negative phase-shift ratios lead to positive and reverse power flows, respectively.

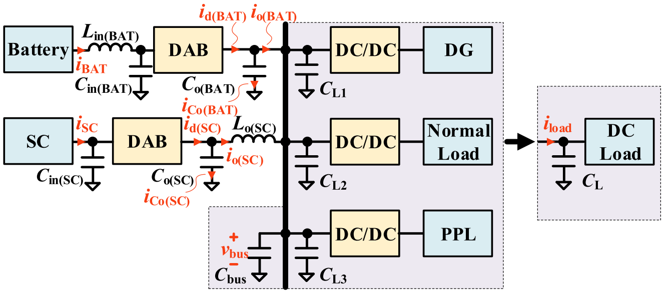

Fig. 3. Architecture of HESS with DAB interface converters.

The architecture of the dc microgrid with HESS and DAB interface converters is depicted in Fig. 3, which contains a DG, normal load, and PPL. As the HESS compensates the total power mismatch between the DG and all loads, the dc microgrid model can be simplified to an HESS supplying a lumped load, as the dashed box in Fig. 3. With the following proposed control strategy, the SC converter is to be simulated to a current source; hence, there is an additional filter inductor, i.e., $L_{\mathrm{o(SC)}}$, set at the output port. Meanwhile, another filter inductor $L_{\mathrm{in(BAT)}}$ set at the input port of the battery converter plays the role of smoothing current ripple for battery life extension [24].

B. AC Component Estimation of Load Current

Although the loads are modeled as lumped, it is not practical to detect total load current, since the loads may be installed in different locations. To extract the ac component, a load current estimator is discussed first.

The steady-state function of the battery converter with droop control is

$$V_{\mathrm{o(BAT)}} = V_{\mathrm{nom}} - R_{\mathrm{dr}} I_{\mathrm{o(BAT)}} \tag{2}$$

where $V_{\mathrm{o(BAT)}}$ and $I_{\mathrm{o(BAT)}}$ are the output voltage and current of the battery converter, respectively, V_{nom} is the nominal bus voltage, and R_{dr} is the droop coefficient.

According to Fig. 3, the current of HESS always equals equivalent load current, namely,

$$i_{\mathrm{load}} = i_{\mathrm{o(BAT)}} + i_{\mathrm{o(SC)}} = I_{\mathrm{d(BAT)}} + i_{\mathrm{Co(BAT)}} + i_{\mathrm{o(SC)}} \tag{3}$$

where i_{load}, $i_{\mathrm{o(BAT)}}$, and $i_{\mathrm{o(SC)}}$ are the total load current, the output current of the battery converter, and the output current of the SC converter, respectively. Besides, $i_{\mathrm{d(BAT)}}$ is the rectified current of the battery converter and $I_{\mathrm{d(BAT)}}$ is its average value; $i_{\mathrm{Co(BAT)}}$ is the current through the output capacitor of the battery converter.

When the power supply and consumption reach a balance, the bus voltage keeps steady; thus, $i_{\mathrm{Co(BAT)}}$ is considered as zero. With the droop characteristics, $I_{\mathrm{d(BAT)}}$ is replaced with

$$I_{\mathrm{d(BAT)}} = I_{\mathrm{o(BAT)}} = (V_{\mathrm{nom}} - V_{\mathrm{bus}})/R_{\mathrm{dr}} \tag{4}$$

where v_{bus} is the bus voltage, and all the capital letters indicate average values of their counterparts.

When the load power changes, $i_{\mathrm{Co(BAT)}}$ is calculated as

$$i_{\mathrm{Co(BAT)}} = C_{\mathrm{o(BAT)}} \frac{dv_{\mathrm{bus}}}{dt} \tag{5}$$

where $C_{\mathrm{o(BAT)}}$ is the output capacitance of the battery converter.

According to (2)–(5), the real load current i_{load} and its estimated value $i_{\mathrm{load(EST)}}$ can be derived as

$$\begin{aligned} i_{\mathrm{load}}(s) &= (V_{\mathrm{nom}} - V_{\mathrm{bus}})/R_{\mathrm{dr}} - sC_{\mathrm{o(BAT)}} v_{\mathrm{bus}}(s) \\ &\quad + i_{\mathrm{o(SC)}}(s) \end{aligned} \tag{6}$$

$$\begin{aligned} i_{\mathrm{load(EST)}}(s) &= \frac{V_{\mathrm{nom}}}{R_{\mathrm{dr}}} - \frac{v_{\mathrm{bus}}(s)}{R_{\mathrm{dr}}} - C_{\mathrm{o(BAT)}} v_{\mathrm{bus}}(s) \frac{\omega_{\mathrm{D}}^2 s}{(s+\omega_{\mathrm{D}})^2} \\ &\quad + i_{\mathrm{o(SC)}}(s) \\ &\triangleq \frac{V_{\mathrm{nom}}}{R_{\mathrm{dr}}} - v_{\mathrm{bus}}(s)\left(\frac{1}{R_{\mathrm{dr}}} + C_{\mathrm{o(BAT)}} G_{\mathrm{2diff}}(s)\right) \\ &\quad + i_{\mathrm{o(SC)}}(s) \end{aligned} \tag{7}$$

where $G_{\mathrm{2diff}}(s)$ is a second-order differentiator and ω_{D} is its corner angular frequency.

Equation (7) needs only local real-time information of v_{bus} and $i_{\mathrm{o(SC)}}$; in addition, the invariable information of V_{nom}, R_{dr}, and $C_{\mathrm{o(BAT)}}$ is known beforehand. Because a typical differentiator s magnifies noises as its high-frequency gain is close to infinity, a second-order differentiator is adapted here, whose frequency-domain characteristics are as follows:

$$\begin{aligned} G_{\mathrm{2diff}}(0^+) &= \frac{\omega_{\mathrm{D}}^2 s}{(s+\omega_{\mathrm{D}})^2}\Big|_{s\to 0^+} = s \\ G_{\mathrm{2diff}}(+\infty) &= \frac{\omega_{\mathrm{D}}^2 s}{(s+\omega_{\mathrm{D}})^2}\Big|_{s\to +\infty} = \frac{\omega_{\mathrm{D}}^2}{s}. \end{aligned} \tag{8}$$

When the angular frequency is lower than ω_{D}, $G_{\mathrm{2diff}}(s)$ acts as a typical differentiator, while when the angular frequency is higher than ω_{D}, $G_{\mathrm{2diff}}(s)$ approximates to an integrator with gain, which could attenuate high-frequency noise.

To extract the ac component of load current, a high-pass filter (HPF) $G_{\mathrm{HPF}}(s)$ is added

$$G_{\mathrm{HPF}}(s) = \frac{s}{s+\omega_{\mathrm{H}}} \tag{9}$$

where ω_{H} is the corner angular frequency of the HPF. Assume that a unit current pulse happens, the high-pass component is supplied by the SC unit, and the rest part is supplied by the battery unit. The ripple of $i_{\mathrm{o(BAT)}}$ after the first pulse can be calculated as

$$\Delta i_{\mathrm{o(BAT)}} = 1 - e^{-\omega_{\mathrm{H}} t_{\mathrm{PPL}}} \leq 1 - e^{-\omega_{\mathrm{H}} \frac{D_{\mathrm{PPL(max)}}}{f_{\mathrm{PPL(min)}}}} \tag{10}$$

where t_{PPL} is the pulse duration, $D_{\mathrm{PPL(max)}}$ is the maximum PPL duty cycle, and $f_{\mathrm{PPL(min)}}$ is the minimum PPL frequency. In this article, $D_{\mathrm{PPL(max)}}$ is 30%; a recommendation selection $\omega_{\mathrm{H}} \leq 0.2\pi f_{\mathrm{PPL(min)}}$ leads to $\Delta i_{\mathrm{o(BAT)}}$ less than 20% of pulse current. One may select a much lower ω_{H} for less $\Delta i_{\mathrm{o(BAT)}}$; however, it also results in very slow response of the HPF [21].

The steady component cannot pass through the HPF; hence, the ac current reference of the SC converter can be simplified as

$$\begin{aligned} i_{\mathrm{ref(SC)}}(s) &= i_{\mathrm{load(EST)}}(s) G_{\mathrm{HPF}}(s) \\ &= \left[-v_{\mathrm{bus}}(s)\left(\frac{1}{R_{\mathrm{dr}}} + C_{\mathrm{o(BAT)}} G_{\mathrm{2diff}}(s)\right)\right. \\ &\quad \left. + i_{\mathrm{o(SC)}}(s)\right] G_{\mathrm{HPF}}(s). \end{aligned} \tag{11}$$

C. Digital Implementations of AC Current Extraction

The bilinear transformation is applied to (11) to obtain

$$G_{\text{2diff}}(z) = G_{\text{2diff}}(s)\big|_{s=\frac{2}{T_{\text{s}}}\frac{1-z^{-1}}{1+z^{-1}}} = \frac{\alpha_0+\alpha_1 z^{-2}}{1+\alpha_2 z^{-1}+\alpha_3 z^{-2}}$$

$$G_{\text{HPF}}(z) = G_{\text{HPF}}(s)\big|_{s=\frac{2}{T_{\text{s}}}\frac{1-z^{-1}}{1+z^{-1}}} = \frac{\alpha_4+\alpha_5 z^{-1}}{1+\alpha_6 z^{-1}}$$

$$i_{\text{ref(SC)}}(z) = \left(-\frac{v_{\text{bus}}(z)}{R_{\text{dr}}} + i_{\text{o(SC)}}(z) - C_{\text{o(BAT)}} v_{\text{bus}}(z) G_{\text{2diff}}(z)\right) G_{\text{HPF}}(z) \quad (12)$$

where T_{s} is the switching and sampling period and α_0–α_6 are expressed as

$$\alpha_0 = 2T_{\text{s}}\omega_{\text{D}}^2/(\omega_{\text{D}}T_{\text{s}}+2)^2,\ \alpha_1 = -2T_{\text{s}}\omega_{\text{D}}^2/(\omega_{\text{D}}T_{\text{s}}+2)^2$$
$$\alpha_2 = 2(\omega_{\text{D}}T_{\text{s}}-2)/(\omega_{\text{D}}T_{\text{s}}+2),\ \alpha_3 = (\omega_{\text{D}}T_{\text{s}}-2)^2/(\omega_{\text{D}}T_{\text{s}}+2)^2$$
$$\alpha_4 = 2/(\omega_{\text{H}}T_{\text{s}}+2),\ \alpha_5 = -2/(\omega_{\text{H}}T_{\text{s}}+2)$$
$$\alpha_6 = (\omega_{\text{H}}T_{\text{s}}-2)/(\omega_{\text{H}}T_{\text{s}}+2). \quad (13)$$

The discretized equations are shown as

$$i_{\text{ref(SC)}}[k] = \alpha_4 x[k] + \alpha_5 x[k-1] - \alpha_6 i_{\text{ref(SC)}}[k-1] \quad (14)$$

where k denotes the kth sampling instant and

$$x[k] = \frac{-v_{\text{bus}}[k]}{R_{\text{dr}}} + i_{\text{o(SC)}}[k] - C_{\text{o(BAT)}} v_{\text{bus\_2diff}}[k]$$
$$v_{\text{bus\_2diff}}[k] = \alpha_0 v_{\text{bus}}[k] + \alpha_1 v_{\text{bus}}[k-2] - \alpha_2 v_{\text{bus\_2diff}}[k-1] - \alpha_3 v_{\text{bus\_2diff}}[k-2]. \quad (15)$$

III. ADRC-BASED AC CURRENT TRACKING

With the ac component extracted, the ac current is set as the reference of the SC converter $i_{\text{ref(SC)}}$. The widely used PI control is powerless in this application of tracking high-frequency $i_{\text{ref(SC)}}$. Though one could substantially increase open-loop crossover frequency for faster tracking ability, however, an enough phase margin (PM) is not guaranteed. In this section, ADRC is applied to the SC converter to satisfy both desired tracking ability and pulsed power distribution.

A. Modeling of SC Converter for Current Tracking

The SC converter is different from the general DAB model with a resistive load [25], there are an extra output inductor $L_{\text{o(SC)}}$ and a dc voltage bus at the output port; in addition, the control target is tracking varying $i_{\text{ref(SC)}}$, instead of regulating voltage.

Considering the case of forward power flow, the piecewise linear equivalent circuits of the DAB converter are depicted in Fig. 4; owing to the symmetry of i_{L} and i_{d}, it is sufficient to consider half a switching period. Note that the equivalent series resistor (ESR) R_{Co} in the output capacitor branch is taken into consideration; because C_{o} and L_{o} form an LC filter, the ESR actually reduces the risk of undamped oscillations.

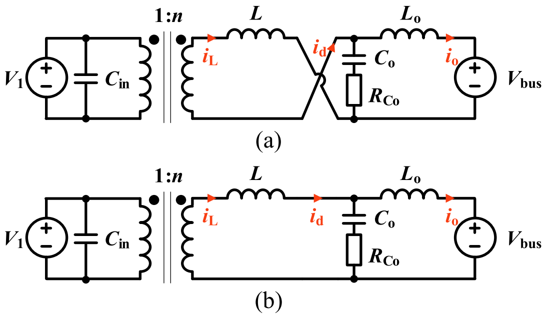

Fig. 4. Piecewise linear equivalent circuits in half a switching period. (a) t_0–t_1. (b) t_1–T_{hs}.

The current of an auxiliary inductor i_{L} is not regarded as a state variable because its average value equals zero in a complete switching period [25]; the reduced second-order state functions are

$$C_{\text{o}}\frac{dv_{\text{Co}}}{dt} = I_{\text{d}} - i_{\text{o}}$$
$$L_{\text{o}}\frac{di_{\text{Lo}}}{dt} = v_{\text{Co}} + R_{\text{Co}}(I_{\text{d}} - i_{\text{o}}) - V_{\text{bus}} \quad (16)$$

where I_{d} is the average value of i_{d} from t_0 to T_{hs}, and it can be derived with the help of (1), as follows:

$$I_{\text{d}} = \frac{nV_1}{2f_{\text{s}}L}D(1-D). \quad (17)$$

The small-signal model can be derived through adding small disturbance into (16) and taking out the average part [26]. The state space of the small-signal model is

$$\begin{bmatrix} \frac{d\hat{v}_{\text{Co}}}{dt} \\ \frac{d\hat{i}_{\text{o}}}{dt} \end{bmatrix} = \begin{bmatrix} 0 & -\frac{1}{C_{\text{o}}} \\ \frac{1}{L_{\text{o}}} & -\frac{R_{\text{Co}}}{L_{\text{o}}} \end{bmatrix} \begin{bmatrix} \hat{v}_{\text{Co}} \\ \hat{i}_{\text{o}} \end{bmatrix} + \begin{bmatrix} -\frac{T_{\text{hs}}nV_1}{LC_{\text{o}}}(2D-1) & 0 \\ -\frac{R_{\text{Co}}T_{\text{hs}}nV_1}{LC_{\text{o}}}(2D-1) & -\frac{1}{L_{\text{o}}} \end{bmatrix} \begin{bmatrix} \hat{d} \\ \hat{v}_{\text{bus}} \end{bmatrix}$$
$$\triangleq A \begin{bmatrix} \hat{v}_{\text{Co}} \\ \hat{i}_{\text{o}} \end{bmatrix} + \begin{bmatrix} B_0 & B_1 \end{bmatrix} \begin{bmatrix} \hat{d} \\ \hat{v}_{\text{bus}} \end{bmatrix}$$
$$\hat{i}_{\text{o}} = \begin{bmatrix} 0 & 1 \end{bmatrix} \begin{bmatrix} \hat{v}_{\text{Co}} \\ \hat{i}_{\text{o}} \end{bmatrix} \triangleq C \begin{bmatrix} \hat{v}_{\text{Co}} \\ \hat{i}_{\text{o}} \end{bmatrix}. \quad (18)$$

According to the control theory, the transfer function from d to i_{o} can be derived as

$$G_{\text{io\_d}}(s) = C(sE-A)^{-1}B_0 = \frac{T_{\text{hs}}nV_1(1-2D)(C_{\text{o}}R_{\text{Co}}s+1)}{(C_{\text{o}}L_{\text{o}}s^2 + C_{\text{o}}R_{\text{Co}}s+1)L} \quad (19)$$

where E is a second-order identity matrix.

B. Principle of ADRC for the SC Converter

By transforming the transfer function into differential equation form and introducing a disturbance ω into it, the standard

ADRC form can be derived as

$$\ddot{i}_{\mathrm{o(SC)}} = -a_0 i_{\mathrm{o(SC)}} - a_1 \dot{i}_{\mathrm{o(SC)}} + a_2 \dot{d} + bd + \omega \tag{20}$$

where

$$a_0 = \frac{1}{L_{\mathrm{o(SC)}} C_{\mathrm{o(SC)}}},\ a_1 = \frac{R_{\mathrm{Co(SC)}}}{L_{\mathrm{o(SC)}}}$$
$$a_2 = \frac{T_{\mathrm{hs}} n V_1 (1-2D) R_{\mathrm{Co(SC)}}}{L_{\mathrm{SC}} C_{\mathrm{o(SC)}}},\ b = \frac{T_{\mathrm{hs}} n V_1 (1-2D)}{L_{\mathrm{SC}} C_{\mathrm{o(SC)}} L_{\mathrm{o(SC)}}}. \tag{21}$$

Note that b is highly related to D, indicating that the dynamic behavior is affected by the operation point. ADRC has the mechanism to eliminate the effect of different operation points by substituting $b = b_0 + \Delta b$, where b_0 represents a presupposed operation point and Δb represents the mismatches caused by varying operation points, modeling errors, and parameters uncertainties, which would be compensated by the Luenberger observer. In this article, the SC converter runs in a bidirectional power flow mode; hence, $D = 0$ is the best compromise when calculating b_0.

By combining $-a_0 i_{\mathrm{o(SC)}} - a_1 \dot{i}_{\mathrm{o(SC)}} + a_2 \dot{d}$, disturbance ω, and modeling mismatches Δbd with the so-called generalized disturbance f, the differential equation of (20) changes to

$$\ddot{i}_{\mathrm{o(SC)}} = b_0 d \underbrace{-a_0 i_{\mathrm{o(SC)}} - a_1 \dot{i}_{\mathrm{o(SC)}} + \Delta bd + a_2 \dot{d} + \omega}_{f}. \tag{22}$$

The crucial concept of ADRC is that if f can be eliminated, the open-loop transfer function of $G_{\mathrm{io(SC)\_d}}(s)$ will be transformed to a second-order integrator system b_0/s^2; then, a simple proportional–differential (PD) controller is enough to balance the tracking and stability performance.

According to the differential equation (22), a newly defined state space with the extended state variable f is derived as

$$\begin{aligned}
\begin{bmatrix} \dot{i}_{\mathrm{o(SC)}} \\ \ddot{i}_{\mathrm{o(SC)}} \\ \dot{f} \end{bmatrix} &= \begin{bmatrix} 0 & 1 & 0 \\ 0 & 0 & 1 \\ 0 & 0 & 0 \end{bmatrix} \begin{bmatrix} i_{\mathrm{o(SC)}} \\ \dot{i}_{\mathrm{o(SC)}} \\ f \end{bmatrix} + \begin{bmatrix} 0 \\ b_0 \\ 0 \end{bmatrix} d + \begin{bmatrix} 0 \\ 0 \\ 1 \end{bmatrix} \dot{f} \\
&\triangleq A_{\mathrm{e}} \begin{bmatrix} i_{\mathrm{o(SC)}} \\ \dot{i}_{\mathrm{o(SC)}} \\ f \end{bmatrix} + B_{\mathrm{e}} d + E_{\mathrm{e}} \dot{f} \\
i_{\mathrm{o(SC)}} &= \begin{bmatrix} 1 & 0 & 0 \end{bmatrix} \begin{bmatrix} i_{\mathrm{o(SC)}} \\ \dot{i}_{\mathrm{o(SC)}} \\ f \end{bmatrix} \triangleq C_{\mathrm{e}} \begin{bmatrix} i_{\mathrm{o(SC)}} \\ \dot{i}_{\mathrm{o(SC)}} \\ f \end{bmatrix}
\end{aligned} \tag{23}$$

where A_{e}, B_{e}, C_{e}, and E_{e} are extended state-space matrices.

Then, a Luenberger observer is set up in the extended state space

$$\begin{aligned}
\begin{bmatrix} \dot{\hat{i}}_{\mathrm{o(SC)}} \\ \ddot{\hat{i}}_{\mathrm{o(SC)}} \\ \dot{\hat{f}} \end{bmatrix} &= A_{\mathrm{e}} \begin{bmatrix} \hat{i}_{\mathrm{o(SC)}} \\ \dot{\hat{i}}_{\mathrm{o(SC)}} \\ \hat{f} \end{bmatrix} + B_{\mathrm{e}} d + \begin{bmatrix} l_{\mathrm{ob1}} \\ l_{\mathrm{ob2}} \\ l_{\mathrm{ob3}} \end{bmatrix} \left(i_{\mathrm{o(SC)}} - \hat{i}_{\mathrm{o(SC)}} \right) \\
&= \left(A_{\mathrm{e}} - L_{\mathrm{ob}} C_{\mathrm{e}} \right) \begin{bmatrix} \hat{i}_{\mathrm{o(SC)}} \\ \dot{\hat{i}}_{\mathrm{o(SC)}} \\ \hat{f} \end{bmatrix} + B_{\mathrm{e}} d + L_{\mathrm{ob}} i_{\mathrm{o(SC)}}
\end{aligned} \tag{24}$$

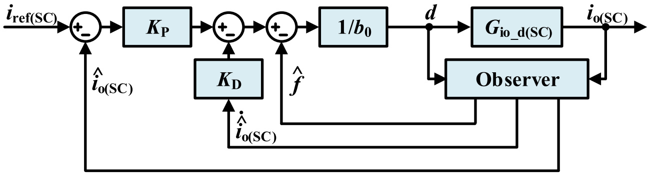

Fig. 5. ADRC-based current tracking of the SC converter.

where $L_{\mathrm{ob}} = [l_{\mathrm{ob1}}, l_{\mathrm{ob2}}, l_{\mathrm{ob3}}]^{\mathrm{T}}$ is the observer vector and the symbol ^ presents the estimated value. Note that $\dot{f}$ does not exist in this observer, which is a common practice in ADRC because f can always be estimated by the correction function of L_{ob} [27], [28], [29], [30].

One can design a PD control law as follows:

$$d = \frac{K_{\mathrm{P}} \left(i_{\mathrm{ref(SC)}} - \hat{i}_{\mathrm{o(SC)}} \right) - K_{\mathrm{D}} \dot{\hat{i}}_{\mathrm{o(SC)}} - \hat{f}}{b_0} \tag{25}$$

with which the closed-loop dynamics is a typical second-order oscillation element if $\hat{f} \approx f$ holds, and it is easy to adjust the dynamic behavior by tuning K_{P} and K_{D}, i.e.,

$$\begin{aligned}
\ddot{i}_{\mathrm{o(SC)}} &= b_0 d + f = K_{\mathrm{P}} \left(i_{\mathrm{ref(SC)}} - \hat{i}_{\mathrm{o(SC)}} \right) - K_{\mathrm{D}} \dot{\hat{i}}_{\mathrm{o(SC)}} - \hat{f} + f \\
&\approx K_{\mathrm{P}} (i_{\mathrm{ref(SC)}} - \hat{i}_{\mathrm{o(SC)}}) - K_{\mathrm{D}} \dot{\hat{i}}_{\mathrm{o(SC)}}.
\end{aligned} \tag{26}$$

With (26), the ADRC-based current tracking of the SC converter is depicted in Fig. 5.

C. Parameter Design of ADRC

The closed-loop dynamic behavior of (26) is transformed to frequency-domain form

$$\begin{aligned}
G_{\mathrm{io(SC)\_ref}}(s) &= \frac{i_{\mathrm{o(SC)}}(s)}{i_{\mathrm{ref(SC)}}(s)} \approx \frac{K_{\mathrm{P}}}{s^2 + K_{\mathrm{D}} s + K_{\mathrm{P}}} \\
&\triangleq \frac{\omega_{\mathrm{n}}^2}{s^2 + 2\zeta \omega_{\mathrm{n}} s + \omega_{\mathrm{n}}^2}
\end{aligned} \tag{27}$$

where ω_{n} and ζ are the oscillation angular frequency and the damping coefficient, respectively. To ensure a smooth current tracking dynamics without overshoot at all operation points, ζ is set to 1.2 in this article; hence

$$K_{\mathrm{P}} = 0.17 K_{\mathrm{D}}^2 \triangleq \omega_{\mathrm{n}}^2. \tag{28}$$

In (27), there are two separated poles located at the real axis in the s-plane; if we ignore the one further away from the origin, the time-domain unit step response of (27) is simplified with

$$h(t) = 1 - e^{(-\zeta + \sqrt{\zeta^2 - 1}) \omega_{\mathrm{n}} t}. \tag{29}$$

Define the settle time t_{set} as the unit step response time that the output reaches 0.98 from 0; with a presupposed ζ, $\omega_{\mathrm{n}} t_{\mathrm{set}}$ can be derived by solving

$$h(t_{\mathrm{set}}) = 1 - e^{(-\zeta + \sqrt{\zeta^2 - 1}) \omega_{\mathrm{n}} t_{\mathrm{set}}} = 0.98. \tag{30}$$

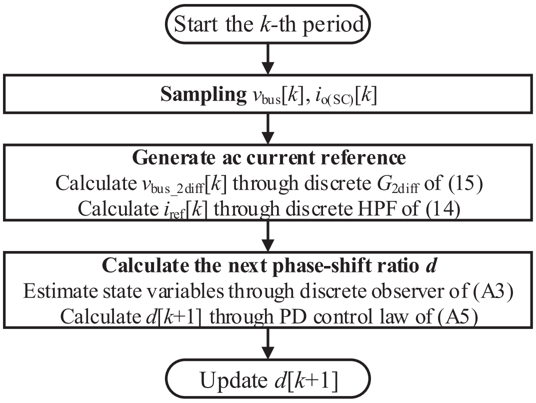

Fig. 6. Flowchart of the SC controller.

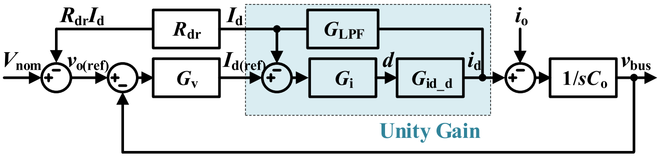

Fig. 7. Droop control scheme of the battery converter.

TABLE I
PARAMETERS OF CONVERTERS

Parameters	Values	Parameters	Values
Nominal input voltage V_1	48 V	Turns ratio of transformer 1:n	1:2
Nominal bus voltage V_{nom}	100 V	Auxiliary inductance L	20 μH
Switching frequency f_s	50 kHz	Equivalent bus capacitance C_{L}	400 μF
Input capacitance C_{in} and ESR	400 μF/50 mΩ	Output capacitance C_{o} and ESR	400 μF/50 mΩ
Input inductance L_{in} and ESR (battery converter)	4.7 μH/10 mΩ	Output inductance L_{o} and ESR (SC converter)	4.7 μH/10 mΩ

*Unless otherwise stated, the battery converter and the SC converter share these parameters.

TABLE II
PARAMETERS OF CONTROLLERS

Controller parameters of the battery converter			
Parameters	Values	Parameters	Values
PI compensator of outer voltage loop $G_{\text{v}}(s)$	1.45 + 32.4/s	PI compensator of inner current loop $G_{\text{i}}(s)$	0.02 + 32.4/s
Cutoff angular frequency of G_{LPF} for I_{d}	6.28E3 rad/s	Droop coefficient R_{dr}	1V/A
Controller parameters of the SC converter			
Parameters	Values	Parameters	Values
Corner angular frequency of second-order differentiator ω_{D}	18.84E3 rad/s	Corner angular frequency of HPF ω_{H}	3.14 rad/s
b_0	2.55E10	Observer l_{ob1}–l_{ob3}	1.88E5/1.18E10/2.47E14
K_{P}	2.07E8	K_{D}	3.49E4

Then, K_{P} and K_{D} can be derived using (28)–(30) as

$$K_{\text{P}} \approx \frac{51.84}{t_{\text{set}}^2}, \quad K_{\text{D}} \approx \frac{17.46}{t_{\text{set}}}. \tag{31}$$

Above discussions are based on the assumptions that the Luenberger observer is fast enough to estimate f, which means that the bandwidth of the observer ω_{ob} should be much larger than ω_{n}. With the bandwidth-parameterization method [31], the triple poles of the observer (24) are located at the same position in the s-plane, i.e., $(-\omega_{\text{ob}}, 0)$. The characteristic polynomial of the observer (24) is

$$\begin{aligned}\det(sE - (A_{\text{e}} - L_{\text{ob}}C_{\text{e}})) &= s^3 + l_{\text{ob1}}s^2 + l_{\text{ob2}}s + l_{\text{ob3}} \\ &\triangleq (s - (-\omega_{\text{ob}}))^3\end{aligned} \tag{32}$$

where

$$l_{\text{ob1}} = 3\omega_{\text{ob}}, \; l_{\text{ob2}} = 3\omega_{\text{ob}}^2, \; l_{\text{ob3}} = \omega_{\text{ob}}^3 \tag{33}$$

generally $\omega_{\text{ob}} = (3 \sim 10)\omega_{\text{n}}$, which is a compromise between fast observation and high-frequency noise sensitivity [32].

All the parameters of the SC controller can be calculated once t_{set} and the presupposed phase-shift ratio D are determined, including b_0, K_{P}, K_{D}, and l_{ob1}–l_{ob3}.

The discrete ADRC derivation and controller law can be found in the Appendix. Fig. 6 shows the complete flowchart of the SC controller.

D. Droop Characteristics of the Battery Converter

Like any other DAB converter with double-loop control, the battery converter commonly takes I_{d} as the inner current loop [33], and the control block is shown in Fig. 7. The inner current loop is regarded as unity gain since its bandwidth should be designed to be much higher than that of the outer voltage loop. The only difference from common droop control is replacing i_{o} with I_{d} in the droop feedback path, which helps to reduce a current sensor.

With a reasonable voltage compensator, the closed-loop bandwidth of the voltage loop could be designed as $\omega_{\text{v(BAT)}} = 1/(R_{\text{dr}}C_{\text{o(BAT)}})$; then, closed-loop output impedance $Z_{\text{oc(BAT)}}(s)$ is shaped to approximately an LPF [34], i.e.,

$$Z_{\text{oc\_APX(BAT)}}(s) = \frac{R_{\text{dr}}\omega_{\text{v(BAT)}}}{s + \omega_{\text{v(BAT)}}}. \tag{34}$$

IV. FREQUENCY-DOMAIN ANALYSIS

Assume that the minimum pulse time is 1 ms, which satisfies a large number of PPLs [35], [36], [37]; there should be enough time margin when selecting t_{set}. Since in the control strategy of the SC converter, the dynamic behavior of $i_{\text{o(SC)}}$ is no longer a simple step response with a constant current reference, but a varying reference, one should accelerate the tracking dynamic to compensate the time delay from the ac current estimation algorithm of (12)–(15). In this article, t_{set} is set to 0.5 ms, the corresponding ω_{n} is 1.44E4 rad/s, and ω_{ob} is selected as 6.28E4 rad/s to attenuate the switching and sampling ripple noises with frequency higher than 10 kHz. Other parameters are listed in Tables I and II.

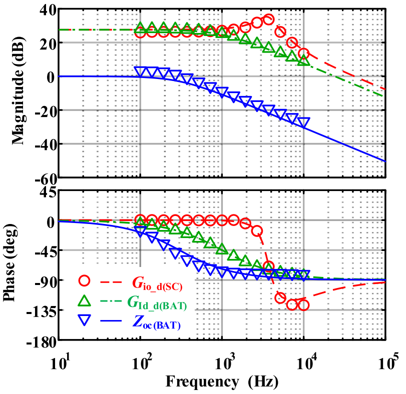

Fig. 8. Modeling verification of transfer functions related to the DAB converter ($D = 0.25$).

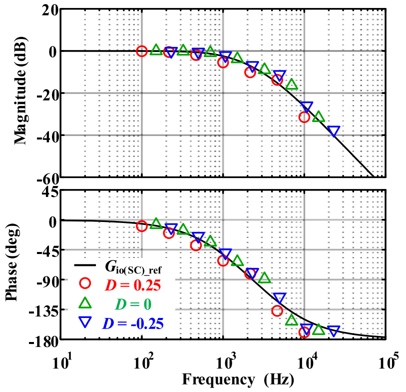

Fig. 9. Verifications of transfer functions $G_{\text{io(SC)\_ref}}$ at different operation points.

A. *Modeling Verification*

Fig. 8 shows the theoretical models and simulation results by the MATLAB/Simulink frequency-sweeping tool. The sweeping results marked by discrete symbols always follow the analytical ones represented by lines, proving that those transfer functions are accurate enough for controller design.

As analyzed before, the observer has the compensation mechanism that makes the current tracking performance consistent even at different operation points. In Fig. 9, the solid line is the theoretical bode plot of $G_{\text{io(SC)\_ref}}$ when ζ equals 1.2; the discrete symbols are frequency-sweeping results, and they match well.

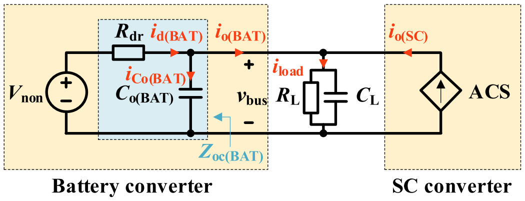

Fig. 10. Simplified system model.

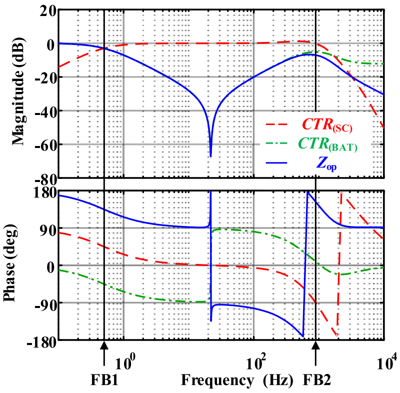

Fig. 11. Bode plots of $CTR_{\text{(SC)}}(s)$, $CTR_{\text{(BAT)}}(s)$, and $Z_{\text{op}}(s)$ with ADRC.

B. *Frequency-Domain Analysis on Power Distribution and Droop Characteristics*

The whole system is further simplified in Fig. 10. As (11) and (27) imply, the SC converter acts as an adaptive current source (ACS) that only tracks ac current. The closed-loop output impedance of the battery converter $Z_{\text{oc(BAT)}}$ can be simplified as $Z_{\text{oc\_APX(BAT)}}$ in (34), and its low-pass characteristics are exactly in line with a voltage source with R_{dr} and $C_{\text{o(BAT)}}$. Define $CTR_{\text{(SC)}}(s)$ and $CTR_{\text{(BAT)}}(s)$ as the current transfer ratio from i_{load} to $i_{\text{o(SC)}}$ and $i_{\text{d(BAT)}}$, respectively, which indicate how much current the SC and battery converters provide to the load. Define $Z_{\text{op}}(s)$ as the parallel output impedance of the two converters, and it determines how the dc bus responds to load current. The following expressions are derived from Fig. 10:

$$\begin{aligned} i_{\text{load}}(s) &= i_{\text{o(BAT)}}(s)+i_{\text{o(SC)}}(s)\\ v_{\text{bus}}(s) &= -\,i_{\text{o(BAT)}}(s)Z_{\text{oc(BAT)}}(s)\\ &\approx -\,i_{\text{o(BAT)}}(s)Z_{\text{oc\_APX(BAT)}}(s)\\ i_{\text{o(SC)}}(s) &= i_{\text{load(EST)}}(s)G_{\text{HPF}}(s)G_{\text{io(SC)\_ref}}(s)\\ i_{\text{o(BAT)}}(s) &= i_{\text{d(BAT)}}(s)+i_{\text{Co(BAT)}}(s). \end{aligned} \tag{35}$$

CTR(s) and $Z_{\text{op}}(s)$ with ADRC can be derived as

$$\begin{aligned} CTR_{\text{(SC)}}(s) &= \frac{i_{\text{o(SC)}}(s)}{i_{\text{load}}(s)} = \frac{\Delta_1\Delta_2}{1-\Delta_1+\Delta_1\Delta_2}\\ CTR_{\text{(BAT)}}(s) &= \frac{i_{\text{o(BAT)}}(s)}{i_{\text{load}}(s)} = \frac{1-\Delta_1}{1-\Delta_1+\Delta_1\Delta_2}\\ Z_{\text{op}}(s) &= \frac{v_{\text{bus}}(s)}{i_{\text{load}}(s)} = \frac{-Z_{\text{oc\_APX(BAT)}}(s)(1-\Delta_1)}{1-\Delta_1+\Delta_1\Delta_2} \end{aligned} \tag{36}$$

where

$$\begin{aligned} \Delta_1 &= G_{\text{HPF}}(s)G_{\text{io(SC)\_ref}}(s)\\ \Delta_2 &= Z_{\text{oc\_APX(BAT)}}(s)\left[\frac{1}{R_{\text{dr}}}+C_{\text{o(BAT)}}G_{\text{2diff}}(s)\right]. \end{aligned} \tag{37}$$

Fig. 11 shows $CTR_{\text{(SC)}}(s)$, $CTR_{\text{(BAT)}}(s)$, and $Z_{\text{op}}(s)$, in which frequency domain is divided into three frequency bands (FBs), where FB1 and FB2 are at 0.5 and 900 Hz, respectively.

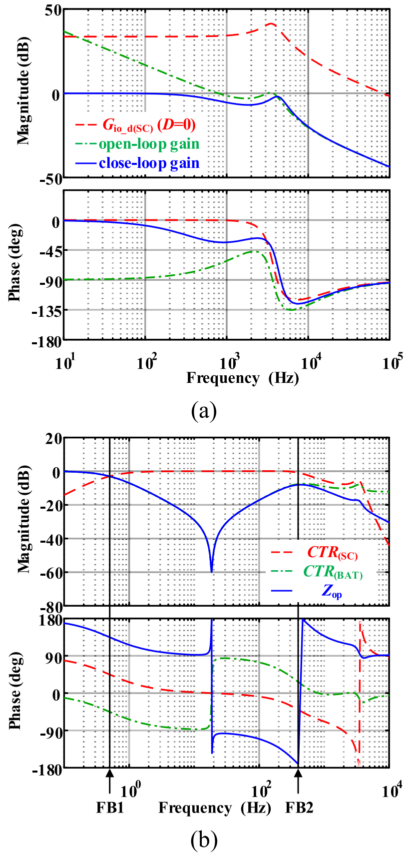

Fig. 12. Frequency-domain characteristics with the PI-compensated SC converter. (a) Bode plots of $G_{\mathrm{io\_d}}(\mathrm{SC})$, open-loop, and closed-loop gains. (b) Bode plots of $CTR_{(\mathrm{SC})}(s)$, $CTR_{(\mathrm{BAT})}(s)$, and $Z_{\mathrm{op}}(s)$.

$CTR_{(\mathrm{SC})}(s)$ shows relatively lower gain than $CTR_{(\mathrm{BAT})}(s)$ when the frequency is lower than FB1, verifying that the very low frequency power is mostly supplied by the battery converter. From FB1 to FB2, $|CTR_{(\mathrm{SC})}(s)|$ is much larger than $|CTR_{(\mathrm{BAT})}(s)|$, leading to that the ac power is mainly supplied by the SC converter. When the frequency is higher than FB2, $|CTR_{(\mathrm{SC})}(s)|$ reduces; because the SC converter could not track the ac current with such high frequency, improving FB2 is crucial to track high-frequency current.

In addition, the dc gain of $Z_{\mathrm{op}}(s)$ equals $20\lg R_{\mathrm{dr}}$, indicating that the droop characteristics of the battery converter are unaffected, even though adding an SC unit to the system.

C. Comparison With a PI Compensator

ADRC shows desired future that the dynamic behaviors are almost coincident at varying operation points, which is favorable for the SC converter, since it frequently changes the operation point when PPL occurs. However, if the PI compensator is used, one should consider PM at different operation points. Fig. 12(a) shows an example of PI design at the operation point $D = 0$, following the principle of PM larger than 60°, and the compensator is $0.008 + 90/s$. The PI compensator necessarily lowers crossover frequency to avoid the resonance peak; finally, the closed-loop bandwidth is about 300 Hz.

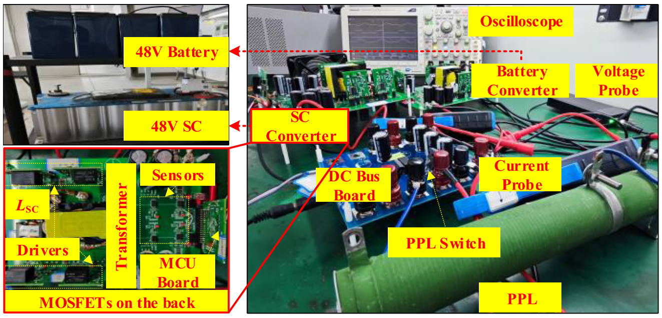

Fig. 13. Experimental testbench.

As a comparison of Fig. 11, Fig. 12(b) shows $CTR(s)$ and $Z_{\mathrm{op}}(s)$ with the PI-compensated SC converter, where FB1 and FB2 are at 0.5 and 400 Hz, respectively; apparently, FB2 of PI control is much lower than that of ADRC, leading to a poorer high-frequency ac current tracking performance.

V. EXPERIMENTAL RESULTS

An experimental testbench is established, as depicted in Fig. 13. The parameters are the same as in Tables I and II. The battery pack consists of four 12 V lead-acid cells in series, and the SC with the capacitance of 165 F is from Maxwell Technology. The converters are controlled by two independent microcontrol units (MCUs) of TMS320F280049 from Texas Instruments, and there is no communication between them. A 10 Ω slide rheostat simulates the PPL and is controlled by a periodically switching MOSFET. The normal load is simulated by an electrical load.

A. Steady Power Distribution and Tracking Performance

Fig. 14(a)–(c) depicts the steady waveforms of the proposed pulse power distribution with ADRC; the duty cycle of PPL is 30%, and the peak power is about 1 kW. When the PPL requires 10 A peak current for an instant, the SC converter immediately outputs 7 A peak current; when the PPL stops intermittently, the output current SC converter $i_{\mathrm{o(SC)}}$ stays at –3 A, proving that the SC converter provides almost all the ac current of PPL. The battery converter, by contrast, only provides a very small portion of pulsed power; the negligible fluctuation of i_{BAT} could confirm it.

Fig. 14(d)–(f) shows the waveforms when the PI compensator is used instead of ADRC. Taking Fig. 14(c) and (f), i.e., the cases of 150 Hz PPL as examples, the SC converter with the PI compensator shows much slower current tracking performance; hence, the battery converter needs to provide more pulse power.

Fig. 15 illustrates similar comparative results when PPL duty cycle is reduced to 15%; the tracking current of the SC converter ranges from –1.5 to 8.5 A. In Fig. 15(c), the tracking time of ADRC is about 1 ms, reaching the peak current just before the PPL stops intermittently. However, in Fig. 15(f), the SC converter with the PI compensator could not reach peak current in time, resulting in larger ac power supply by the battery converter and larger dc bus fluctuation.

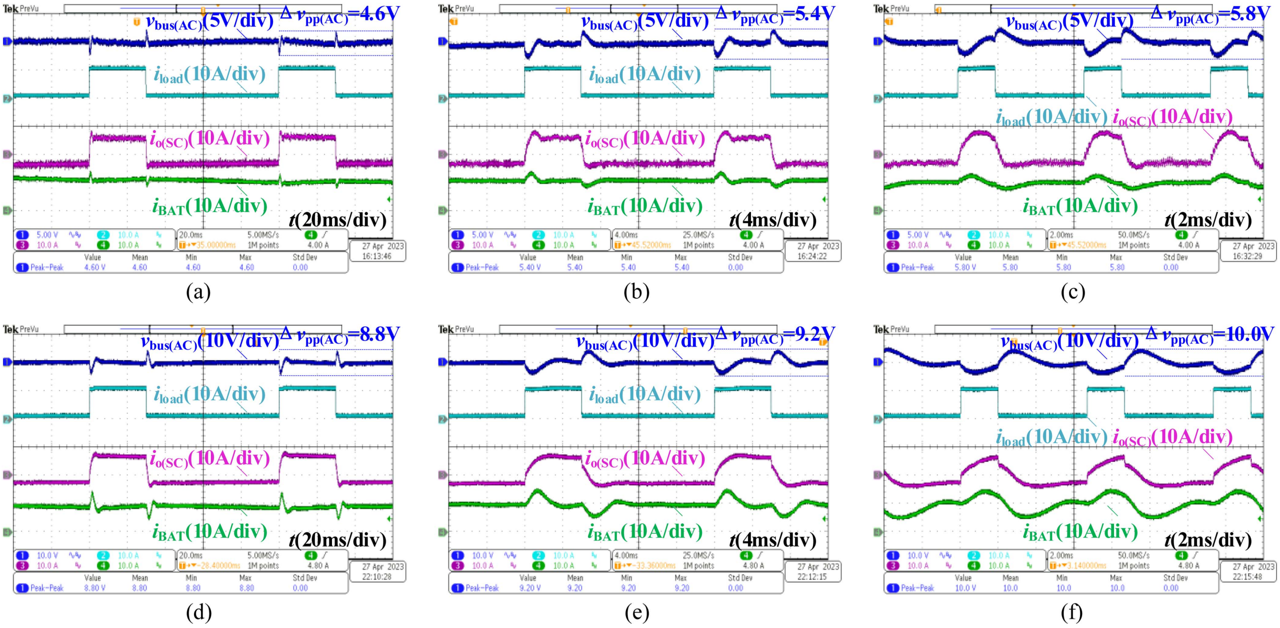

Fig. 14. Steady test; PPL duty cycle is 30%. (a) 10 Hz, ADRC. (b) 50 Hz, ADRC. (c) 150 Hz, ADRC. (d) 10 Hz, PI. (e) 50 Hz, PI. (f) 150 Hz, PI.

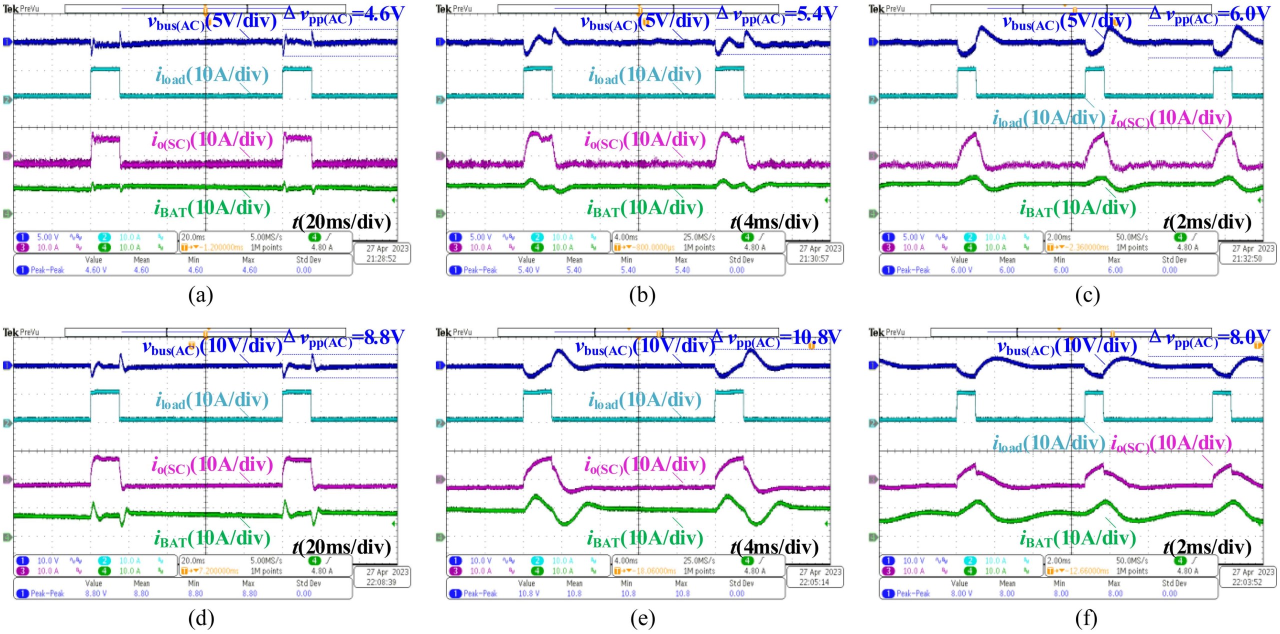

Fig. 15. Steady test; PPL duty cycle is 15%. (a) 10 Hz, ADRC. (b) 50 Hz, ADRC. (c) 150 Hz, ADRC. (d) 10 Hz, PI. (e) 50 Hz, PI. (f) 150 Hz, PI.

To clearly compare the influence of different controls to the dc bus, the ac coupling of the oscilloscope is used while measuring bus voltage fluctuation (the first channels in Figs. 14 and 15). Table III lists the peak-to-peak dc bus voltage fluctuation; ADRC demonstrates advantages over the PI compensator under all tested PPLs. However, in the case of 150 Hz PPL frequency and 15% duty cycle, ADRC demonstrates a smaller performance advantage, because neither of them could track the pulse less than 1 ms.

TABLE III
DC BUS FLUCTUATION COMPARISON WITH DIFFERENT CONTROLS

PPL characteristics		Controls		Bus voltage fluctuation reduction by ADRC
Frequency	Duty cycle	ADRC	PI	
10 Hz	30%	4.6 V	8.8 V	47.7%
	15%	5.4 V	9.2 V	41.3%
50 Hz	30%	5.8 V	10.0 V	42.0%
	15%	4.6 V	8.8 V	47.7%
150 Hz	30%	5.4 V	10.0 V	46.0%
	15%	6.0 V	8.0 V	25.0%

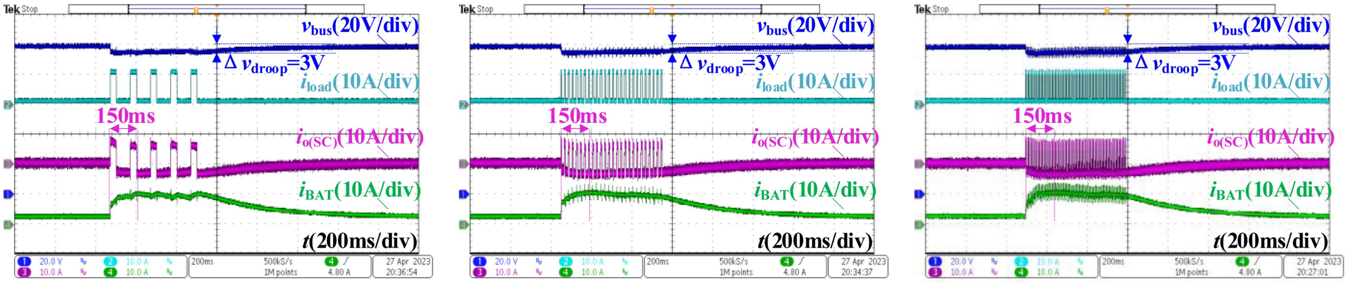

(a) (b) (c)

Fig. 16. Dynamic test; PPL duty cycle is 30%. (a) 10 Hz. (b) 50 Hz. (c) 150 Hz.

TABLE IV
COMPARISON OF POWER DISTRIBUTION METHODS

Power distribution methods	Steady-transient distribution		DC–AC distribution
Implementation	LPF [10], [38]	Virtual capacitor [17],[18], [39]	Adaptive current source (this article)
Design complexity	Low	High	Medium
Implementation complexity	Low	Low	Medium
Communication	Not free	Free	Free
Adapt to PPL	Not	Only adaptation to very low frequency PPL	Adaptation to PPL with wide frequency range
Constraints	LPF with very low corner frequency deteriorates the recovery of bus voltage	Impedance-based parameter design requires repeated debugging [17]	Performance highly relies on the power tracking method
Applications	Centralized dc microgrid without PPL	Distributed dc microgrid with/without very low frequency PPL	Distributed dc microgrid affected by PPL

B. Dynamic Power Distribution and Tracking Performance

Fig. 16 depicts the dynamic distribution and tracking waveforms under different PPL frequencies; the duty cycle and PPL running time are fixed at 30% and 500 ms, respectively. About 150 ms after the first power pulse, the ac component estimation algorithm gets the ac current reference, and the SC converter has caught up with it; meanwhile, the battery converter provides more dc power to maintain power balance. Because the dc current of PPL is 3 A and the droop coefficient R_{dr} is set to 1 V/A, the bus voltage reduces by 3 V. When PPL stops, the bus voltage is restored to the original value. The experimental results indicate that the droop characteristics of the battery converter are unaffected when PPL is in the system.

C. Dynamic Performance When Only Normal Load Works

Fig. 17 shows the waveforms when only normal load is in the system. When the normal load jumps from 1 to 4 A, the SC converter immediately supplies transient power, and battery current i_{BAT} rises slowly until a new steady state, avoiding the transient current surge outflowing the battery pack. Owing to the droop characteristics, there is a 3 V bus voltage reduction.

The experimental result indicates that the proposed power distribution method is not only for PPL but also suitable for the case where PPL stops and only normal load works.

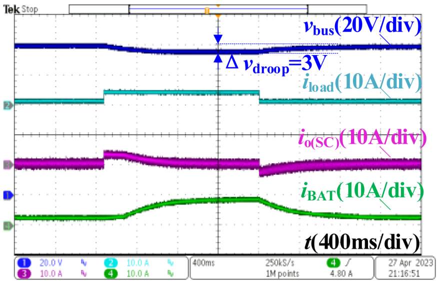

Fig. 17. Experimental waveform when only normal load works.

VI. COMPARISONS AND DISCUSSIONS

The proposed control strategy is a combination of power distribution and tracking methods. Table IV compares the power distribution methods. The methods based on the LPF and the virtual capacitor require SC converter handling transient power, which is only a small part of varying power, resulting in that these methods can only be used when the load contains no or very low frequency periodical power; otherwise, most of the periodical power would be still provided by the battery unit. On the contrary, with the dc–ac distribution, all periodical power is handled by the SC unit; thus, the advantages of the HESS are fully exploited.

However, dc–ac distribution necessarily requires a fast controller for the SC converter, because it always tracks step power

TABLE V
COMPARISON OF POWER TRACKING METHODS

Power tracking methods	LQR [6]	MPC [38], [41], [42]	DBC [40], [43]	ADRC (this article)
Design complexity	Medium	High	Low	Medium
Implementation complexity	Low	High	Low	Medium
Performance	Slow and accurate	Fast and with steady error [41]	Fast and with overshoot	Fast and accurate
Robustness	Robust, parameter mismatch is acceptable	Medium, relies on model accuracy, needs additional compensation [42]	Poor, heavily relies on parameter accuracy, needs additional parameter identification [43]	Robust, parameter mismatch is eliminated by the observer

if PPL occurs. Table V compares ADRC with other advanced controls. Though the nonlinear controllers, such as MPC and DBC, show outstanding performance, however, the performance often deteriorates due to model and parameter inaccuracies. Besides, the calculation burdens of MPC and DBC with parameter identification require a very high performance MCU. In contrast, ADRC shows better tracking performance than PI control and LQR control, with the robustness against model and parameter uncertainties.

Therefore, the combination of dc–ac power distribution and ADRC could be a simple and effective method for the HESS supplying PPL in a distributed dc microgrid.

VII. CONCLUSION

This article proposed a communication-free pulsed power distribution and tracking method for the HESS in a dc microgrid, which is based on the concept of dc–ac component. A well-designed SC converter with ADRC could track ac component of PPL, and the battery converter only provided the dc component, avoiding the dc bus suffering from large-scale and periodical fluctuation. Moreover, the droop characteristics of the battery converter were unaffected. With the frequency-domain analysis, the principle of power distribution mechanism was illustrated. The experimental results of two DAB converters supplying 10–150 Hz PPL validated the effectiveness of the proposed power distribution method, system modeling, and controller designs.

APPENDIX

This appendix provides a brief derivation of discrete-time ADRC, and a more detailed derivation can be found in [27] and [32].

To avoid confusion, the superscript ~ represents the predicted state variables based on the model, and the superscript ^ represents the corrected ones by the observer. The prediction and correction processes are expressed as

$$\tilde{x}[k] = A_{\mathrm{d}}\hat{x}[k-1] + B_{\mathrm{d}}d[k-1] \tag{A1}$$

$$\hat{x}[k] = \tilde{x}[k] + L_{\mathrm{d}}(y[k] - C_{\mathrm{d}}\tilde{x}[k]) \tag{A2}$$

where $\tilde{x} = [\tilde{i}_{\mathrm{o(SC)}}\ \dot{\tilde{i}}_{\mathrm{o(SC)}}\ \tilde{f}]^{\mathrm{T}}$, $\hat{x} = [\hat{i}_{\mathrm{o(SC)}}\ \dot{\hat{i}}_{\mathrm{o(SC)}}\ \hat{f}]^{\mathrm{T}}$, A_{d}, B_{d}, and C_{d} are transformed from their discrete-time counterparts in (24) through zero-order-hold discretization, and L_{d} is the discrete gain vector of the current observer.

Substituting (A1) into (A2), the complete discrete observer is derived as

$$\begin{aligned}\hat{x}[k] = {} & (A_{\mathrm{d}} - L_{\mathrm{d}}C_{\mathrm{d}}A_{\mathrm{d}})\hat{x}[k-1] + (B_{\mathrm{d}} - L_{\mathrm{d}}C_{\mathrm{d}}B_{\mathrm{d}})d[k-1] \\ & + L_{\mathrm{d}}y[k].\end{aligned} \tag{A3}$$

The desired observer poles in the s-plane are designed at $(-\omega_{\mathrm{ob}}, 0)$ and then mapped to the z-plane via $z_{\mathrm{ob}} = e^{-\omega_{\mathrm{ob}}T_{\mathrm{s}}}$. Similar to the continue observer that the poles are set in a same location, the discrete observer follows that

$$\det(zE - (A_{\mathrm{d}} - L_{\mathrm{d}}C_{\mathrm{d}}A_{\mathrm{d}})) \triangleq (z - z_{\mathrm{ob}})^3. \tag{A4}$$

By solving (A4), L_{d} is obtained. According to the control law in (25), the phase-shift ratio calculated in the kth period is

$$d[k] = \frac{K_{\mathrm{P}}(i_{\mathrm{ref(SC)}}[k] - \hat{i}_{\mathrm{o(SC)}}[k]) - K_{\mathrm{D}}\dot{\hat{i}}_{\mathrm{o(SC)}}[k] - \hat{f}[k]}{b_0}. \tag{A5}$$

REFERENCES

[1] N. A. Sevostyanov and R. L. Gorbunov, “Control strategy to mitigate voltage ripples in droop-controlled dc microgrids,” *IEEE Trans. Power Electron.*, vol. 38, no. 12, pp. 15377–15389, Dec. 2023.

[2] J. Tian, F. Wang, F. Zhuo, and H. Deng, “A full-power-range optimization scheme under double-side asymmetrical phase-shift modulation in DAB-based distributed energy storage system,” *IEEE J. Emerg. Sel. Topics Power Electron.*, early access, doi: 10.1109/JESTPE.2023.3255517.

[3] Q. Sun, S. Chen, L. Chen, and D. Ma, “Quasi-Z-source network-based hybrid power supply system for aluminum electrolysis industry,” *IEEE Trans. Ind. Inform.*, vol. 13, no. 3, pp. 1141–1151, Jun. 2017.

[4] L. Zhou, J. Zhou, Q. Liu, J. Zhao, F. Huang, and Z. Zhu, “Dynamic power balancing control method for energy storage DC/DC parallel supply system with low-frequency pulsed load,” *IEEE Trans. Ind. Electron.*, early access, doi: 10.1109/TIE.2023.3296825.

[5] S. Jin et al., “A high-drive-performance microsecond pulse power module for portable DBD plasma source device,” *IEEE Trans. Power Electron.*, vol. 38, no. 12, pp. 15072–15085, Dec. 2023.

[6] P. Xia, H. Shi, H. Wen, Q. Bu, Y. Hu, and Y. Yang, “Robust LMI-LQR control for dual-active-bridge DC–DC converters with high parameter uncertainties,” *IEEE Trans. Transp. Electrific.*, vol. 6, no. 1, pp. 131–145, Mar. 2020.

[7] L. Chen, S. Shao, Q. Xiao, L. Tarisciotti, P. W. Wheeler, and T. Dragicevic, “Model predictive control for dual-active-bridge converters supplying pulsed power loads in naval dc micro-grids,” *IEEE Trans. Power Electron.*, vol. 35, no. 2, pp. 1957–1966, Feb. 2020.

[8] M. Bahloul and S. K. Khadem, “Impact of power sharing method on battery life extension in HESS for grid ancillary services,” *IEEE Trans. Energy Convers.*, vol. 34, no. 3, pp. 1317–1327, Sep. 2019.

[9] X. Chang, Y. Li, X. Li, and X. Chen, "An active damping method based on a supercapacitor energy storage system to overcome the destabilizing effect of instantaneous constant power loads in dc microgrids," *IEEE Trans. Energy Convers.*, vol. 32, no. 1, pp. 36–47, Mar. 2017.

[10] U. Manandhar, N. R. Tummuru, S. K. Kollimalla, A. Ukil, G. H. Beng, and K. Chaudhari, "Validation of faster joint control strategy for battery- and supercapacitor-based energy storage system," *IEEE Trans. Ind. Electron.*, vol. 65, no. 4, pp. 3286–3295, Apr. 2018.

[11] Y. Yan, Q. Li, W. Huang, and W. Chen, "Operation optimization and control method based on optimal energy and hydrogen consumption for the fuel cell/supercapacitor hybrid tram," *IEEE Trans. Ind. Electron.*, vol. 68, no. 2, pp. 1342–1352, Feb. 2021.

[12] B. Hredzak, V. G. Agelidis, and M. Jang, "A model predictive control system for a hybrid battery-ultracapacitor power source," *IEEE Trans. Power Electron.*, vol. 29, no. 3, pp. 1469–1479, Mar. 2014.

[13] B. Wang, U. Manandhar, X. Zhang, H. B. Gooi, and A. Ukil, "Deadbeat control for hybrid energy storage systems in dc microgrids," *IEEE Trans. Sustain. Energy*, vol. 10, no. 4, pp. 1867–1877, Oct. 2019.

[14] Y. Zhang and Y. W. Li, "Energy management strategy for supercapacitor in droop-controlled DC microgrid using virtual impedance," *IEEE Trans. Power Electron.*, vol. 32, no. 4, pp. 2704–2716, Apr. 2017.

[15] X. Chen, P. Yang, Y. Peng, M. Wang, F. Hu, and J. Xu, "Output voltage drop and input current ripple suppression for the pulse load power supply using virtual multiple quasi-notch-filters impedance," *IEEE Trans. Power Electron.*, vol. 38, no. 8, pp. 9552–9565, Aug. 2023.

[16] J. Xiao, P. Wang, and L. Setyawan, "Hierarchical control of hybrid energy storage system in dc microgrids," *IEEE Trans. Ind. Electron.*, vol. 62, no. 8, pp. 4915–4924, Aug. 2015.

[17] Q. Xu et al., "A decentralized dynamic power sharing strategy for hybrid energy storage system in autonomous dc microgrid," *IEEE Trans. Ind. Electron.*, vol. 64, no. 7, pp. 5930–5941, Jul. 2017.

[18] M. Zhang, Q. Xu, C. Zhang, L. Nordström, and F. Blaabjerg, "Decentralized coordination and stabilization of hybrid energy storage systems in dc microgrids," *IEEE Trans. Smart Grid*, vol. 13, no. 3, pp. 1751–1761, May 2022.

[19] X. Zhao, Y. W. Li, H. Tian, and X. Wu, "Energy management strategy of multiple supercapacitors in a dc microgrid using adaptive virtual impedance," *IEEE J. Emerg. Sel. Topics Power Electron.*, vol. 4, no. 4, pp. 1174–1185, Dec. 2016.

[20] P. Gao, Y. Li, M. Huang, W. Yao, X. Zheng, and C. Zhang, "An energy storage equipment sizing process based on static and dynamic characteristics for pulsed power load in airborne electrical power system," *IEEE Trans. Transp. Electrific.*, early access, doi: 10.1109/TTE.2023.3303213.

[21] X. Huang, X. Ruan, F. Du, F. Liu, and L. Zhang, "A pulsed power supply adopting active capacitor converter for low-voltage and low-frequency pulsed loads," *IEEE Trans. Power Electron.*, vol. 33, no. 11, pp. 9219–9230, Nov. 2018.

[22] L. Xu, S. Zhuo, J. Liu, S. Jin, Y. Huangfu, and F. Gao, "Advancement of active disturbance rejection control and its applications in power electronics," *IEEE Trans. Ind. Appl.*, early access, doi: 10.1109/TIA.2023.3312653.

[23] N. Hou and Y. W. Li, "Overview and comparison of modulation and control strategies for a nonresonant single-phase dual-active-bridge dc–dc converter," *IEEE Trans. Power Electron.*, vol. 35, no. 3, pp. 3148–3172, Mar. 2020.

[24] K. Uddin, A. D. Moore, A. Barai, and J. Marco, "The effects of high frequency current ripple on electric vehicle battery performance," *Appl. Energy*, vol. 178, pp. 142–154, Sep. 2016.

[25] S. Shao et al., "Modeling and advanced control of dual active bridge dc-dc converters: A review," *IEEE Trans. Power Electron.*, vol. 37, no. 2, pp. 1524–1547, Feb. 2022.

[26] X. Yue, X. Wang, and F. Blaabjerg, "Review of small-signal modeling methods including frequency-coupling dynamics of power converters," *IEEE Trans. Power Electron.*, vol. 34, no. 4, pp. 3313–3328, Apr. 2019.

[27] R. Miklosovic, A. Radke, and Z. Gao, "Discrete implementation and generalization of the extended state observer," in *Proc. IEEE Amer. Control Conf.*, 2006, pp. 2209–2214.

[28] J. Li, Y. Han, S. Zhou, Z. Li, H. Fan, and B. Wang, "Improved linear active disturbance rejection control with dynamic event-triggered mechanism for hybrid energy storage system," *IEEE Trans. Transp. Electrific.*, early access, doi: 10.1109/TTE.2023.3300334.

[29] L. Feng, X. Sun, Z. Yang, and K. Diao, "Optimal torque sharing function control for switched reluctance motors based on active disturbance rejection controller," *IEEE/ASME Trans. Mechatron.*, vol. 28, no. 5, pp. 2600–2608, Oct. 2023.

[30] L. Tao, P. Wang, X. Ma, Y. Wang, and X. Zhou, "Variable form LADRC-based robustness improvement for electrical load interface in microgrid: A disturbance response perspective," *IEEE Trans. Ind. Inform.*, early access, doi: 10.1109/TII.2023.3265534.

[31] Z. Gao, "Scaling and bandwidth-parameterization based controller tuning," in *Proc. Amer. Control Conf.*, 2003, pp. 4989–4996.

[32] G. Herbst, "Practical active disturbance rejection control: Bumpless transfer, rate limitation, and incremental algorithm," *IEEE Trans. Ind. Electron.*, vol. 63, no. 3, pp. 1754–1762, Mar. 2016.

[33] F. Xiong, J. Wu, Z. Liu, and L. Hao, "Current sensorless control for dual active bridge dc–dc converter with estimated load-current feedforward," *IEEE Trans. Power Electron.*, vol. 33, no. 4, pp. 3552–3566, Apr. 2018.

[34] G. Liu, P. Mattavelli, and S. Saggini, "Resistive–capacitive output impedance shaping for droop-controlled converters in dc microgrids with reduced output capacitance," *IEEE Trans. Power Electron.*, vol. 35, no. 6, pp. 6501–6511, Jun. 2020.

[35] M. K. Behera and L. C. Saikia, "A novel resilient control of grid-integrated solar PV-hybrid energy storage microgrid for power smoothing and pulse power load accommodation," *IEEE Trans. Power Electron.*, vol. 38, no. 3, pp. 3965–3980, Mar. 2023.

[36] E. Peng et al., "A pulsed power supply based on an optimized SFPFN scheme producing large currents with a flat top on a heavily inductive load," *IEEE Trans. Power Electron.*, vol. 36, no. 10, pp. 11221–11233, Oct. 2021.

[37] M. Farhadi and O. Mohammed, "Adaptive energy management in redundant hybrid DC microgrid for pulse load mitigation," *IEEE Trans. Smart Grid*, vol. 6, no. 1, pp. 54–62, Jan. 2015.

[38] X. Liu, Y. Suo, Z. Zhang, X. Song, and J. Zhou, "A new model predictive current control strategy for hybrid energy storage system considering the SOC of the supercapacitor," *IEEE J. Emerg. Sel. Topics Power Electron.*, vol. 11, no. 1, pp. 325–338, Feb. 2023.

[39] X. Chen, J. Zhou, M. Shi, L. Yan, W. Zuo, and J. Wen, "A novel virtual resistor and capacitor droop control for HESS in medium-voltage DC system," *IEEE Trans. Power Syst.*, vol. 34, no. 4, pp. 2518–2527, Jul. 2019.

[40] S. Wei, Z. Zhao, K. Li, L. Yuan, and W. Wen, "Deadbeat current controller for bidirectional dual-active-bridge converter using an enhanced SPS modulation method," *IEEE Trans. Power Electron.*, vol. 36, no. 2, pp. 1274–1279, Feb. 2021.

[41] X. Zhang, B. Wang, D. Gamage, and A. Ukil, "Model predictive and iterative learning control based hybrid control method for hybrid energy storage system," *IEEE Trans. Sustain. Energy*, vol. 12, no. 4, pp. 2146–2158, Oct. 2021.

[42] Y. Li, S. Sahoo, T. Dragičević, Y. Zhang, and F. Blaabjerg, "Stability-oriented design of model predictive control for DC/DC boost converter," *IEEE Trans. Ind. Electron.*, vol. 71, no. 1, pp. 922–932, Jan. 2024.

[43] T.-Q. Duong and S.-J. Choi, "Deadbeat control with bivariate online parameter identification for SPS-modulated DAB converters," *IEEE Access*, vol. 10, pp. 54079–54090, 2022.

Lunbo Deng (Student Member, IEEE) was born in Sichuan Province, China, in 1996. He received the B.S. degree in electrical engineering and automation in 2018 from Southwest Jiaotong University, Chengdu, China, where he is currently working toward the Ph.D. degree in electrical engineering.

He is a visiting scholar with McMaster University, Hamilton, ON, Canada, from 2023 to 2024. His current research interests include modeling and control of a bidirectional converter in energy storage systems and microgrids.

Guohua Zhou (Senior Member, IEEE) received the B.S. degree in electronic and information engineering and the M.S. and Ph.D. degrees in electrical engineering from Southwest Jiaotong University, Chengdu, China, in 2005, 2008, and 2011, respectively.

From March 2010 to September 2010, he was a Research Assistant with the Department of Electronic and Information Engineering, Hong Kong Polytechnic University, Kowloon, Hong Kong. From 2010 to 2011, he was a Visiting Scholar (also a joint Ph.D. student) with the Center for Power Electronics Systems, Virginia Polytechnic Institute and State University, Blacksburg, VA, USA. He is currently a Professor with the School of Electrical Engineering, Southwest Jiaotong University. His current research interests include modulation and control techniques of power electronics systems, modeling and stability analysis of switching power converters, and renewable energy applications of power electronics.

Dr. Zhou was the recipient of the National Excellent Doctoral Dissertation of China in 2014. He became a Fellow of the Institution of Engineering and Technology in 2018. He is an Associate Editor for *CPSS Transactions on Power Electronics and Applications*.

Yanglong Li was born in Sichuan Province, China, in 1999. He received the B.S. degree in electrical engineering and automation in 2021 from Southwest Jiaotong University, Chengdu, China, where he is currently working toward the M.S. degree in electrical engineering.

His research interests include high-efficiency isolated dc–dc converters.

Zhengge Chen (Member, IEEE) received the B.S. and M.S. degrees in electrical engineering from Southwest Jiaotong University (SWJTU), Chengdu, China, in 2013 and 2016, respectively, and the Ph.D. degree in energy technology from Aalborg University, Aalborg, Denmark, in 2021.

He was an Assistant Engineer with Huawei Technologies Company, Ltd., Shenzhen, China, from 2016 to 2017. He was a Research Assistant with The Hong Kong Polytechnic University, Hong Kong, in 2017. He was a Visiting Scholar with Virginia Polytechnic Institute and State University, Blacksburg, VA, USA, in 2020. He is currently an Assistant Professor with SWJTU. Since February 2023, he has also been a Mainland–Hong Kong Joint Postdoctoral Fellow with the City University of Hong Kong, Hong Kong. His research interests include power converter topology and control, component modeling, magnetic integration, and reliability analysis.